PHYSICS

Origin of photoinduced DC current and two-level population dynamics in a single molecule

Jiang Yao[1], Youngwook Park[1], Wenlu Shi[1], Siyu Chen[1], W. Ho[1,2]*

Studying the photoinduced changes of materials with atomic-scale spatial resolution can provide a fundamental understanding of light-matter interaction. A long-standing impediment has been the detrimental thermal effects on the stability of the tunneling gap from intensity-modulated laser irradiation of the scanning tunneling microscope junction. Photoinduced DC current transduces photons to an electric current and is widely applied in optoelectronics as switches and signal transmission. Our results revealed the origin of the light-induced DC current and related it to the two-level population dynamics and related nonlinearity in the conductance of a single molecule. Here, we compensated for the near-visible laser-induced thermal effects to demonstrate photoinduced DC current spectroscopy and microscopy and to observe the persistent photoconductivity of a two-level pyrrolidine molecule. The methodology can be generally applied to the coupling of light to scan probes to investigate light-matter interactions at the atomic scale.

INTRODUCTION

Photoinduced DC current is the DC electrical response to light and has been widely observed in macroscopic nonlinear systems (*1*–*5*) and metallic tunneling junctions with near-field plasmon enhancement (*6*, *7*). In addition, single-molecule spectroscopy based on photoinduced DC current measurements in the terahertz and RF frequencies can reach ultrahigh energy and spatial resolution when combined with scanning tunneling microscopy (STM) (*8*–*16*). In these measurements, the intensity modulation combined with lock-in detection was applied to extract the weak photoinduced DC current. However, the intensity modulation of light from mid-infrared (IR) to ultraviolet frequencies introduces a long-standing problem of thermal effects that causes instabilities in the STM tunneling gap (*6*, *17*). A detailed study also directly showed that, with a chopped laser, the thermally induced mechanical oscillation was the major contribution to the optically induced electrical signal of a tip-sample tunneling junction (*18*). To date, two studies circumvented the "thermal problem" and reported photoinduced DC current in STM coupled to IR and visible radiation by using either high-frequency modulation (*19*) or weak laser power (*20*). However, high modulation frequency requires high laser power (>100 mW) because of the large attenuation at high frequencies of the high-gain preamplifier used in STM measurement. Such high laser power can destabilize the tunneling junction and desorb target molecules. Using weak power (<100 μW) limits studies to systems with large photocurrent response and extinction ratio, possibly for electronic states. A universal solution to the "thermal problem" would broaden the use of scan probes to implement photoinduced DC current spectromicroscopy at the atomic scale.

Persistent photoconductivity (PPC) is a phenomenon associated with the persistence of the photoinduced conductance change after the removal of light irradiation (*21*–*24*). Such effect has been widely observed in semiconductors and applied to photodetectors (*25*, *26*), memory devices (*27*, *28*), radiation detection (*29*, *30*), and solar cells (*31*–*33*). The recent observation of the PPC effect in monolayer transition metal dichalcogenides material could reduce the thickness of these photoelectronics (*34*–*36*). The miniaturization in all dimensions may rely on single molecules performing as key elements. However, the PPC effect of a single molecule has not been found. The PPC effect of the semiconducting system can all be attributed to the long lifetime of photoexcited carriers (*21*–*36*). Because of the absence of periodic structure, single molecules often lack energy bands, and the concept of carriers in single molecules is ill-defined. Therefore, the observation of PPC in single molecules requires the invention of a new mechanism.

RESULTS

Here, we demonstrated the Z-compensation technique to counter the laser modulation-induced "thermal problem" of the STM junction instability. We applied a synchronized tip oscillation perpendicular to the sample surface to compensate for the thermally induced tunneling gap oscillation due to chopping of the continuous wave (CW) laser light (Fig. 1A). The laser heating did not require compensation in directions parallel to the surface. The tip oscillation amplitude was tuned to be the same as the tunneling gap oscillation but with a 180° phase difference to nullify the thermal effect (see the Supplementary Materials for the compensation details). The best compensation conditions were achieved by minimizing the tunneling current oscillation amplitude over the substrate surface (background) (Fig. 1B). Such conditions were then used to measure photoinduced DC current over the molecule.

To demonstrate the effectivity of the Z-compensation method, we measured 785-nm CW light-induced DC current over a single pyrrolidine molecule adsorbed on the Cu(001) surface at 6 K with a home-built STM. We observed clear tunneling current oscillations in the total DC current (STM tunneling current plus photoinduced DC current) with laser intensity modulation and proper Z-compensation (Fig. 1B). Theoretically, the chopping method with a square wave modulates the laser intensity and introduces a mechanical oscillation of the tunneling gap with higher harmonic components. However, we found that higher harmonic compensation is not necessary for the measurement because the thermal expansion of the tunnel junction slowly responded to the temperature change.

[1]Department of Physics and Astronomy, University of California, Irvine, Irvine, CA 92697-4575, USA. [2]Department of Chemistry, University of California, Irvine, Irvine, CA 92697-2025, USA.
*Corresponding author. Email: wilsonho@uci.edu

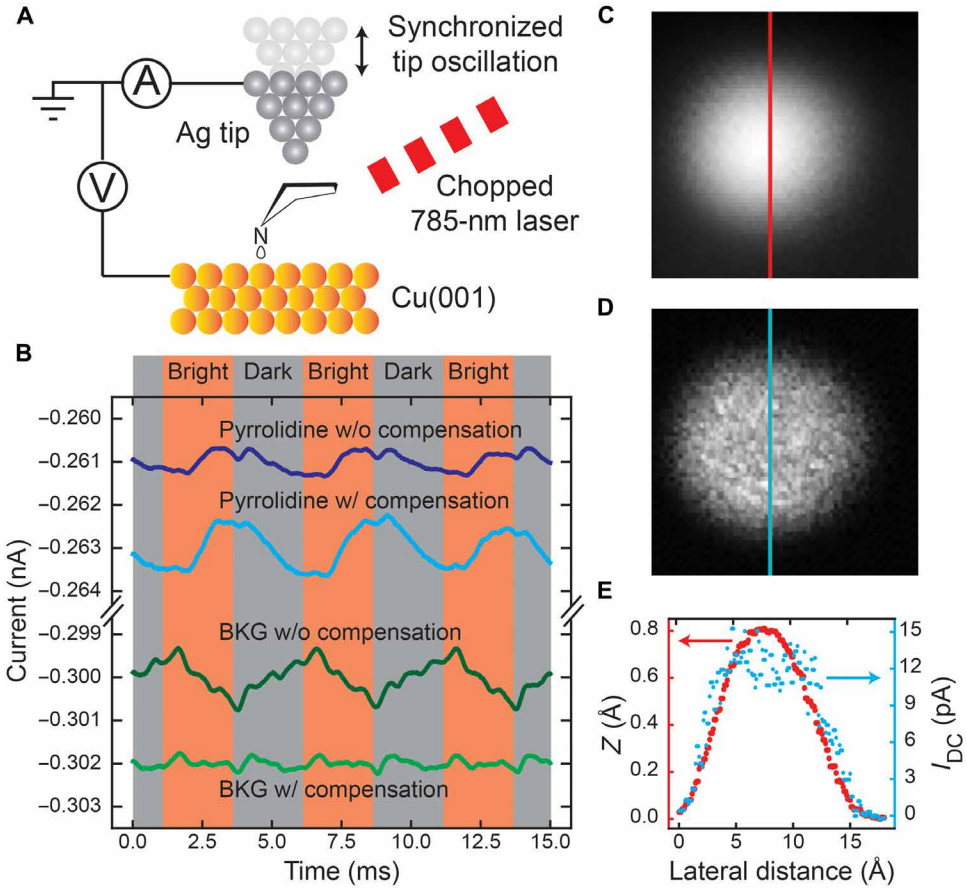

Fig. 1. Atomic-scale photoinduced DC current measurement. (**A**) Schematic diagram of STM photoinduced DC current measurement. The synchronized tip oscillation was used to compensate for the oscillatory thermal expansion of the tunneling gap induced by laser chopping. (See the Supplementary Materials for details of the compensation procedures.) (**B**) Current traces taken over a pyrrolidine molecule and over the Cu(001) background with (w/) and without (w/o) Z-compensation. Before measurement, the feedback loop was first opened at −250 mV/0.75 nA, followed by ramping the sample bias to −100 mV. A constant 3.15-mW CW laser was first chopped at 201 Hz and then focused into the STM junction, and a 12.8-pm amplitude tip oscillation with a phase shift of 74.2° was used for the Z-compensation. All traces in (B) were averaged 20,000 passes. (**C**) Topography and (**D**) photoinduced DC current of pyrrolidine simultaneously imaged. (See the Supplementary Materials for measurement and image processing details.) The photoinduced DC current was measured at a constant conductance set by −250 mV/0.75 nA, followed by ramping the bias to −100 mV. The amplitudes of laser power modulation and Z-oscillation were 0.48 mW and 3.7 pm, respectively. The phase shift for Z-oscillation was 86.0°. We chopped the laser at 327 Hz for all photoinduced DC current measured with lock-in amplifier unless specified otherwise. (**E**) Vertical line cut of (C) (red) and (D) (blue) with red and blue arrows pointing to the corresponding *y* axis. Data in (C) to (E) were obtained with a different tip than the one for data in (B).

Such a slow response acted as a low pass filter and attenuated all higher harmonic temperature oscillations (see fig. S6D). In addition, the slow response of the photoinduced electric current signal also proved that the thermally induced mechanical oscillation was the major contribution to the background signal. Other photo-assisted electrical transport mechanisms, such as hot electron photocurrent, are expected to have a much faster response.

The topography of the molecule is shown in Fig. 1C. The weak photoinduced DC current signal was extracted from the total current with a lock-in amplifier and a two-dimensional mapping of the photoinduced DC current signal was obtained (Fig. 1D). These images exhibit submolecular contrast (Fig. 1, C to E). The topography shows round protrusion, while the photoinduced DC current image exhibits a donut shape with a small dip at the central plateau. We further investigated the origin and relation of the photoinduced DC current to the molecular dynamic response by comparing the results of the experiment to modeling based on single-molecule two-state switching. The line shape of photoinduced DC current spectra also provides direct evidence of the single-molecule PPC effect, which is driven by a novel mechanism of photo-assisted molecular conformational switching.

The laser chopping method with lock-in detection measures photoinduced DC current, I_{DC}, which should reflect the current difference between constant laser irradiation (bright) and without laser irradiation (dark). However, the measured I_{DC} as a function of sample bias [$I_{DC}(V)$; Fig. 2A] differs from the bright $I(V)$ subtracting the dark $I(V)$ [$I_{sub}(V) = I_{bright}(V) - I_{dark}(V)$], in Fig. 2 (B and C). On the other hand, both the $I_{DC}(V)$ (Fig. 2A) and $I_{sub}(V)$ (Fig. 2C) differ from the measured $\frac{d^2I}{dV^2}$ [Fig. 2D, from the conventional inelastic electron tunneling spectroscopy (IETS)]. Furthermore, we did not observe I_{DC} signal over a carbon monoxide (CO) molecule adsorbed on Cu(001), which exhibited a strong $\frac{d^2I}{dV^2}$ (IETS) signal below 50 mV (see fig. S9). Both phenomena suggest that the optical field plays a minor role in the measured pyrrolidine photoinduced DC current

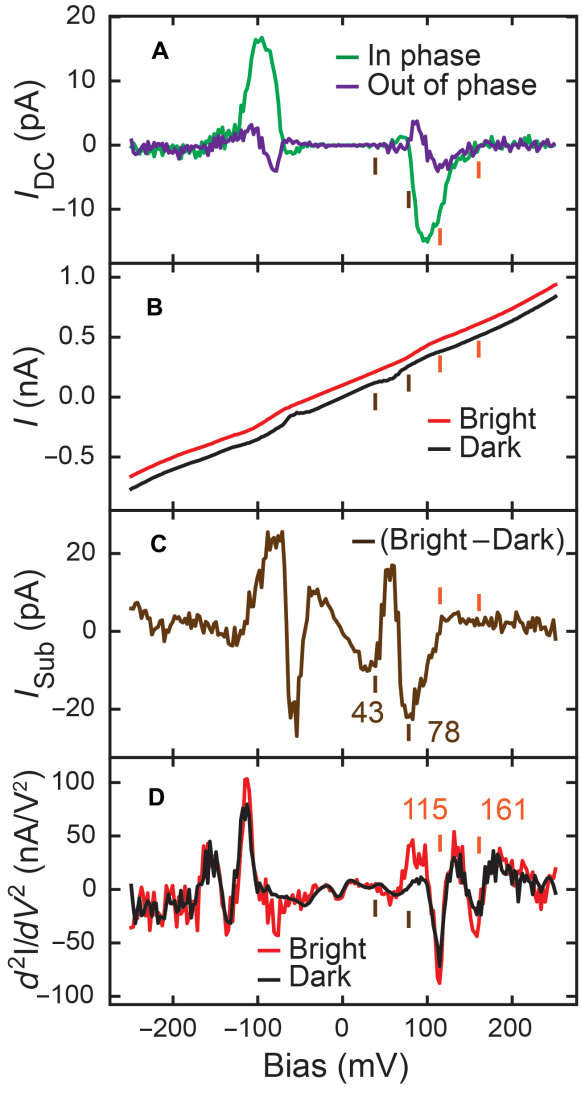

Fig. 2. $I_{DC}(V)$ and $I_{sub}(V)$ of a pyrrolidine molecule on Cu(001). (**A**) $I_{DC}(V)$ of pyrrolidine with 0.97-mW modulated laser power and 8.1-pm Z-oscillation amplitude with a phase shift of 97.7°. (**B**) $I(V)$ of pyrrolidine with constant 0.97-mW unmodulated laser illumination (bright) and without laser illumination (dark). There was a 300-ms wait time before measuring each data point. The bright current is shifted up by 0.1 nA for clarity. (**C**) The result of bright current subtracting dark current in (B). (**D**) IETS (*40*) of pyrrolidine under the same dark and bright conditions as (B). We used 7 mV_{rms} at 397.48-Hz bias modulation for IETS measurement. (A), (B), and (D) were measured over the center of the pyrrolidine molecule, with a constant tunneling gap feedback set point −250 mV/0.75 nA. The short orange and brown lines indicate the dip positions in (B) and (D).

(*6*–*9*, *37*). Therefore, to understand the observed photoinduced DC current, we need to answer two questions: (i) Why does the $I_{DC}(V)$ deviate from the $I_{sub}(V)$? (ii) What is the origin of the I_{DC} and I_{sub}? The out-of-phase signal (Fig. 2A) indicates that the signal phase of I_{DC} varies as the bias changes. Such phase variation implies varying system dynamic responses at different biases, requiring an understanding of the dynamics of the pyrrolidine molecule.

To understand the origin of the I_{DC} and I_{sub}, we investigate the behavior of pyrrolidine molecule at larger tip-molecule separation. The telegraphic noise in low-bias topography (Fig. 3A) supports the switching of pyrrolidine between two conformational states (H and L), the single-molecule states, as depicted in Fig. 3B (*38*–*41*). Current traces monitor such switching process and show two current levels (Fig. 3C). The high and low current levels correspond to H and L states (Fig. 3B). The state residence time, $t_{L/H}$, follows Poisson distribution, which appears as an exponential decay in its probability density function (Fig. 3D). The decay rate defines the corresponding transition rate, $W_{L/H\rightarrow H/L}$, which equals the inverse of the mean value of $t_{L/H}$ (*42*). Such exponential decay suggests that the escaping rate out of the corresponding state equals $n_{L/H}W_{L/H\rightarrow H/L}$ (*43*, *44*), where $n_{L/H}$ is the probability of molecule in the L (H) state. Therefore, combined with probability conservation, a differential equation (Eq. 1) models the response of pyrrolidine switching dynamics.

$$\frac{\partial}{\partial t}\begin{bmatrix} n_H(V,t) \\ n_L(V,t) \end{bmatrix} = \begin{bmatrix} -W_{H\rightarrow L}(V,t) & W_{L\rightarrow H}(V,t) \\ W_{H\rightarrow L}(V,t) & -W_{L\rightarrow H}(V,t) \end{bmatrix}\begin{bmatrix} n_H(V,t) \\ n_L(V,t) \end{bmatrix} \quad (1)$$

To solve for $n_{H/L}$ in Eq. 1, we measured $W_{L/H\rightarrow H/L}$ under dark and bright conditions. The inelastic tunneling electron-assisted switching dominates the dark transition rates (*42*, *45*–*47*), $W_{L/H\rightarrow H/L,dark}$, and the fitted results based on this model agree with the measurement (Fig. 4A). By adding 395.5 and 211.4 Hz to the fitted dark transition rates of $L \rightarrow H$ and $H \rightarrow L$ processes, we produce the solid curves in Fig. 4B, which agrees with the experimentally measured bright transition rates, $W_{L/H\rightarrow H/L,bright}$. Such good fitting indicates voltage-independent light assistance to the pyrrolidine switching process. We also find such light-assisted switching rates to be tip-dependent, which indicates the possible involvement of tip enhanced plasmon effect (*48*, *49*). For time-invariant transition rates $W_{L/H\rightarrow H/L}$, the steady-state solution of Eq. 1 gives the percentage of occupation in the H and L states

$$n_{H/L,\infty}(V) = \frac{W_{L/H\rightarrow H/L}(V)}{W_{L\rightarrow H}(V) + W_{H\rightarrow L}(V)} \quad (2)$$

The difference between bright and dark transition rates leads to different $n_{H/L,\infty}(V)$ (Fig. 4C).

On the other hand, linear relations of state-resolved $I(V)$ (Fig. 4D) suggest constant H and L conductances (σ_H and σ_L) which are insensitive to light irradiation. We extract the σ_H and σ_L from the slope of the corresponding state I-V curve in Fig. 4D, which are 0.658 and 0.174 nS. Therefore, the total tunneling current can be written as follows

$$I(V) = \left[n_H(V)\sigma_H + n_L(V)\sigma_L\right]V = \left[n_H(V)\,\Delta\sigma + \sigma_L\right]V \quad (3)$$

$\Delta\sigma$ is the conductance difference between H and L states, $\sigma_H - \sigma_L$. The final expression in Eq. 3 makes use of the normalization condition of state probability, $n_H + n_L = 1$. Because the laser radiation can induce the change in $n_H(V)$ (Fig. 4C) and the change in $n_H(V)$ contributes to the current change (Eq. 3), we deduce that the photoinduced DC current originates from a light-induced change in population $n_H(V)$.

To verify our deduction, we further calculate the I_{sub} (V) by incorporating the fitted transition rate data (green dashed curve in Fig. 4, A and B) into Eqs. 2 and 3. Figure 5A shows the excellent agreement between the calculated $I_{sub}(V)$ (solid line) and measurement (dots). Next, we focus on revealing the reason for the deviation

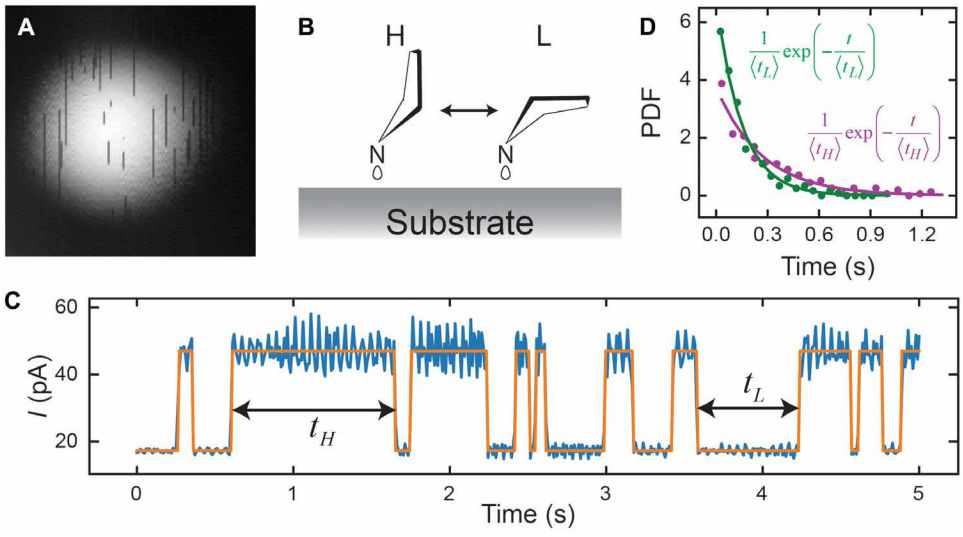

Fig. 3. Switching dynamics of pyrrolidine on Cu(001). (**A**) Constant current topography of pyrrolidine at feedback set point −30 mV/100 pA. (**B**) Schematic of pyrrolidine conformational switching between H and L states. (**C**) Time trace of the tunneling current over the topographic center of pyrrolidine. High and low currents indicate H and L states. Before measurement, a feedback loop was opened after setting the tunneling gap at −250 mV/100 pA, followed by ramping the bias to 73 mV. (**D**) The probability density function of residence time for H (purple) and L (green) states. The statistical data were generated from two current traces of 100-s duration, measured with the same conditions as (C). The solid curves are Poisson distributions calculated from the formula displayed in the same color. $\langle t_H \rangle = 267$ ms and $\langle t_L \rangle = 149$ ms are the mean values of t_H and t_L.

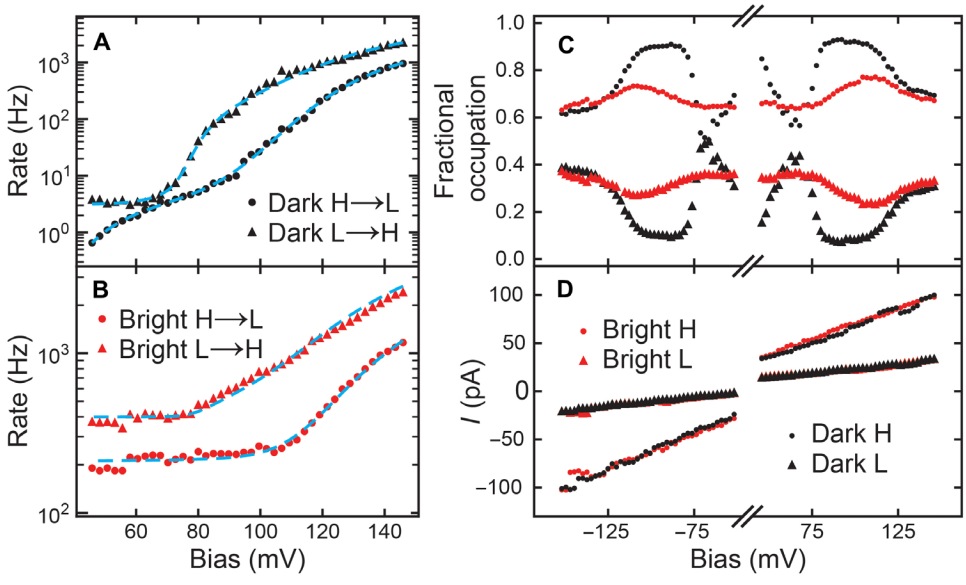

Fig. 4. Bias-dependent switching dynamics of pyrrolidine on Cu(001). (**A** and **B**) Transition rates as a function of sample bias under dark (black) and bright (irradiation with unmodulated, constant 0.97-mW laser, red) conditions. The negative bias data are not shown because of limited space and are presented in the Supplementary Materials. The blue dashed lines in (A) fit the data based on the inelastic tunneling electron switching model. $H \rightarrow L$ rate (dot) was fitted with out-of-plane ring mode (43.3 mV) and ring breathing mode (120.4 mV). $L \rightarrow H$ rate (triangle) was fitted with in-plane ring mode (77.9 mV) and ring breathing mode (111.0 mV). (See the Supplementary Materials for the fitting details.) The mode softening between two different conformations could contribute to the different excitation energies for the same mode. The blue dashed lines in (B) are shifted up by a constant from the corresponding lines in (A): $H \rightarrow L$ by 200 Hz and $L \rightarrow H$ by 380 Hz. (**C**) Occupation percentage as a function of bias for the H (dot) and L (triangle) states of pyrrolidine under bright and dark conditions. (**D**) State-resolved tunneling current under bright and dark conditions measured over the topographic center of pyrrolidine. All statistics displayed in (A) to (D) were extracted from multiple long current traces at each bias with the same tunneling gap set as Fig. 3C.

of I_{DC} (V) from I_{sub} (V). One major difference between I_{DC} (V) and I_{sub} (V) arises from the dynamics of the pyrrolidine conformational change. Here, I_{sub} (V) is the difference in the DC current between two steady-state conditions, bright and dark, while I_{DC} (V) measures the time-dependent changes in the DC current induced by the laser intensity modulation. Laser intensity modulation adds time dependence to the $W_{L/H\rightarrow H/L}$ expression

$$W_{L/H\rightarrow H/L}(V,t) = W_{L/H\rightarrow H/L,\mathrm{dark}}(V) + W_{L/H\rightarrow H/L,\mathrm{ph}}h(t) \quad (4)$$

The square wave function, $h(t)$, oscillates between 0 and 1 at laser power modulation frequency, $\frac{\omega}{2\pi}$. $W_{L/H\rightarrow H/L,\mathrm{ph}}$ is the photon contribution to the transition rates and equals $W_{L/H\rightarrow H/L,\mathrm{bright}} - W_{L/H\rightarrow H/L,\mathrm{dark}}$. The origin of $W_{L/H\rightarrow H/L,\mathrm{ph}}$ likely involves the decay of localized surface plasmons to generate hot electrons that excite pyrrolidine vibrations directly between the two levels in a double-well potential to facilitate the switching process (see the Supplementary Materials).

Adopting $W_{L/H\rightarrow H/L}(V, t)$ form in Eq. 4 and using the fitted dark and bright transition rates in Fig. 4 (A and D), we numerically calculate $n_H(V, t)$ using Eq. 1 and plug it into Eq. 3 to obtain the time-dependent changes in the tunneling current $I(V, t)$. The lock-in measurement extracts the first harmonic component of $I(V, t)$ at the laser power modulation frequency, $I_{DC}(V)$. The calculated $I_{DC}(V)$ using the above method agrees with the experimental measurement (Fig. 5B). Therefore, $I_{DC}(V)$ reflects the dynamic n_H response to a square wave chopped laser illumination. Both I_{DC} and I_{sub} originate from the n_H response to the laser radiation, while their spectral shape exhibits different features. To understand such differences, we further calculate the time evolution of n_H at four different biases (Fig. 5C).

At low biases [40 mV (red) and 67 mV (purple)], $W_{L/H\rightarrow H/L,\mathrm{ph}}$ is notably larger than $W_{L/H\rightarrow H/L,\mathrm{dark}}$. The bright and dark $n_{H,\infty}$ will differ from each other as long as $\frac{W_{L\rightarrow H,\mathrm{dark}}}{W_{H\rightarrow L,\mathrm{dark}}} \neq \frac{W_{L\rightarrow H,\mathrm{ph}}}{W_{H\rightarrow L,\mathrm{ph}}}$ (Eq. 2). Finite values for I_{sub} arise from this difference (Eq. 3). However, I_{DC} reflects n_H variation under the irradiation of chopped laser in the tunneling junction. Upon chopping the laser for intensity modulation, n_H starts to exponentially approach $n_{H,\infty}$ at a rate of $W_{H\rightarrow L} + W_{L\rightarrow H}$ (Fig. 5C, see also equation 7 in the Supplementary Materials). However, before the next laser intensity change, n_H only has limited time to evolve during half of the modulation period. If this half period is much longer than the exponential decay time constant, $1/(W_{H\rightarrow L} + W_{L\rightarrow H})$], n_H can reach its equilibrium value. But the half modulation period that we used is 1.53 ms, thus n_H can only have limited variation and correspondingly near-zero I_{DC}. We describe the signal attenuation due to the slow system response as the dynamical attenuation. We can expect this if the modulation frequency is sufficiently low or the molecule switches at a high rate such as at high bias, I_{DC} approaches I_{sub}.

At a high bias [200 mV (blue)], the inelastic tunneling electron contribution to the transition rates is much higher than the photon contribution, which yields $W_{L/H\rightarrow H/L,\mathrm{dark}} \approx W_{L/H\rightarrow H/L,\mathrm{bright}}$ and correspondingly negligible n_H difference between bright and dark conditions (Eq. 2). Therefore, both I_{DC} and I_{sub} are close to zero.

At an intermediate bias [109 mV (green)], $W_{L/H\rightarrow H/L,\mathrm{ph}}$ is comparable to $W_{L/H\rightarrow H/L,\mathrm{dark}}$, which can introduce a difference in $n_{H,\infty}$ between dark and bright. The dynamic attenuation effect is still not

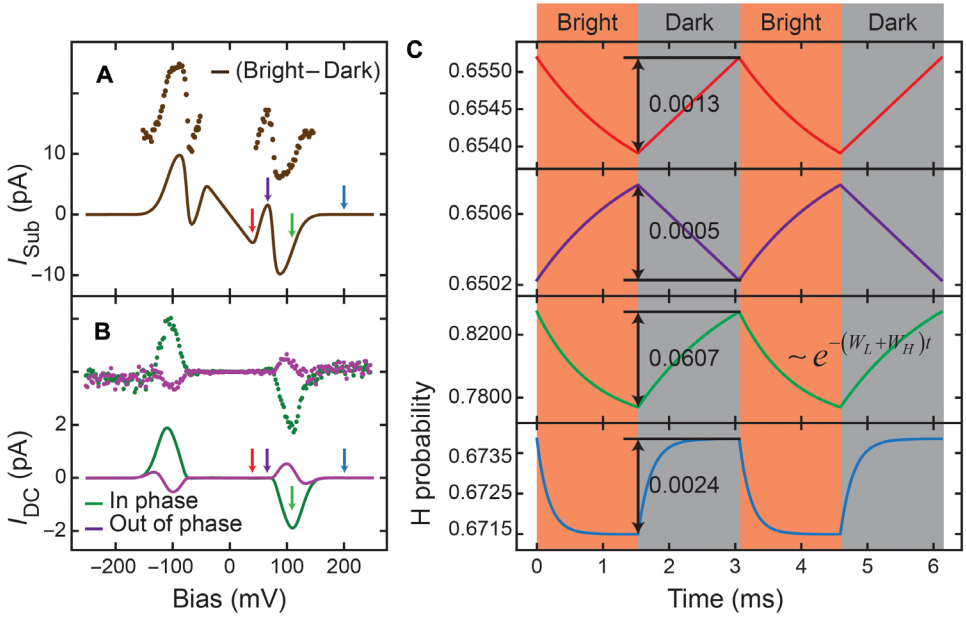

Fig. 5. Origin of photoinduced DC current of pyrrolidine on Cu(001). (**A**) The simulated (solid lines) and measured (dots) results of current under bright conditions subtracting current under dark conditions. The bright and dark currents were measured by averaging the same current traces used for statistics in Fig. 4 (A and B). (**B**) The simulated (solid lines) and measured (dots) $I_{DC}(V)$. The measured $I_{DC}(V)$ were acquired with modulated 0.97-mW laser power, 8.1-pm Z-oscillation amplitude with a phase shift of 81.8° and a constant tunneling gap determined by feedback set point of −250 mV/0.75 nA. The experimental data in (A) and (B) are shifted up by 15 and 4 pA for clarity. (**C**) Simulated time evolution of pyrrolidine H state probability at different sample biases: 40 mV (red), 67 mV (purple), 109 mV (green), and 200 mV (blue). The four biases are also indicated in (A) and (B) with corresponding color arrows. Note the different vertical scales.

too severe to entirely suppress the signal. Therefore, the I_{DC} overall appears as a peak. In addition, if the laser chopping frequency is low enough, n_H can reach the corresponding $n_{H,\infty}$ in each half of the modulation cycle and its time evolution approaches square wave instead of triangular function, which results in $I_{DC} \approx I_{sub}$. Therefore, $I_{DC}(V)$ becomes $I_{sub}(V)$ at a low chopping frequency, equivalent to a low pass filtering effect. In practice, we observe decay in I_{DC} as the chopping frequency increases (see fig. S6C).

From the above analysis, we can conclude that the spectral difference between I_{DC} and I_{sub} originates from the slow n_H response to laser radiation. In this process, the tunneling conductance determined by n_H (Eq. 3) persists a while after switching on and off the light, which reflects the single-molecule PPC effect of pyrrolidine. On the other hand, the I_{DC} measurements exhibit strong dependences on the tunneling current (see fig. S7) and sample bias (Fig. 2A). These dependencies suggest that the single-molecule PPC effect can be controlled by the electron current and energy.

Any laser characteristics that affect the transition rates can potentially change I_{DC} by changing $n_{H,\infty}$ and the dynamic response of the molecule (see the Supplementary Materials). For example, change in laser power and polarization can affect the transition rate and lead to change in $I_{DC}(V)$ (see fig. S8). In addition, the response of the molecular transition rate exhibits laser wavelength dependence (*50*) and the time delay between two ultrafast pump-probe laser pulses (*38*). Therefore, we expect I_{DC} to vary with photon energy and pump-probe delay time, which could serve as spectroscopic tools to characterize single-molecule coherence and dynamics in the frequency and time domains.

DISCUSSION

In summary, we implement a Z-compensation technique to suppress laser-induced thermal instability of the STM junction and measure the dynamic photoinduced DC current of a single pyrrolidine molecule. Such photoinduced DC current originates from changes in the two-state occupation induced by photon-assisted conformational switching. The inverse of the total switching rate exhibited by the molecule determines the response time of the state occupation probability. Such finite single-molecule response leads to the different spectral line shapes between photoinduced DC current arising from the intensity modulation of the fixed frequency laser and the subtraction of the steady-state DC currents for bright and dark. Inelastic tunneling electrons and photons simultaneously induce the two-state switching dynamics for a single molecule. Photoinduced DC current is expected in other photo-switching molecular systems. The Z-compensation technique solves the long-standing thermal problem caused by laser irradiation of the scan probe junction and enables the study of single-molecule dynamics and spectromicroscopy based on the measurement of photoinduced DC current at optical frequencies.

MATERIALS AND METHODS

The experiments were performed using a home-built ultrahigh vacuum STM operating at 6 K. The microscope was cooled by a continuous flow liquid helium cryostat (ARS, Helitran LT3B) with helium supplied by a flexible transfer line connected to a 100-liter dewar. The tips used in the experiments were prepared by electrochemical etching of a 0.051-cm diameter silver wire and subsequent in-vacuum cycles of sputtering with Ne^+ (8×10^{-5} torr) and annealing. The Cu(001) surface was cleaned by cycles of Ne^+ sputtering, followed by annealing to around 800 K. The pyrrolidine chemical (98% purity, Spectrum Chemical) was purified by around 50 freeze-pump-thaw cycles. The molecules at room temperature were evaporated onto Cu(001) surface held at 6 K.

A tunable CW diode laser (DFB pro, TOPTICA) was used to generate 785-nm wavelength light. The laser beam was directed into an acoustic optical modulator to control and chop the laser intensity (fig. S1). The chopped laser beam was focused into the tunneling junction with a 7.6-cm focal length fused silica lens.

Supplementary Materials

This PDF file includes:

Supplementary Text
Figs. S1 to S10
Tables S1 and S2
References

REFERENCES AND NOTES

1. G. D'Amico, G. Pesce, G. Rusciano, A. Sasso, A DFG spectrometer at for high resolution molecular spectroscopy and trace gas detection. *Opt. Lasers Eng.* **37**, 481–493 (2002).
2. B. Bozzini, B. Busson, G. Pietro De Gaudenzi, C. Mele, A. Tadjeddine, An SFG and DFG investigation of polycrystalline Au, Au–Cu and Au–Ag–Cu electrodes in contact with aqueous solutions containing KCN. *J. Alloys Compd.* **427**, 341–349 (2007).
3. B. Bozzini, B. Busson, G. Pietro De Gaudenzi, C. Mele, A. Tadjeddine, An SFG and DFG investigation of Au(111), Au(100), Au(110) and Au(210) electrodes in contact with aqueous solutions containing KCN. *J. Solid State Electrochem.* **12**, 303–313 (2008).
4. B. Bozzini, A. Bund, B. Busson, C. Humbert, A. Ispas, C. Mele, A. Tadjeddine, An SFG/DFG investigation of CN- adsorption at an Au electrode in 1-butyl-1-methyl-pyrrolidinium bis(trifluoromethylsulfonyl) amide ionic liquid. *Electrochem. Commun.* **12**, 56–60 (2010).
5. J. Vogelsang, J. Robin, B. Piglosiewicz, C. Manzoni, P. Farinello, S. Melzer, P. Feru, G. Cerullo, C. Lienau, P. Groß, High passive CEP stability from a few-cycle, tunable NOPA-DFG system for observation of CEP-effects in photoemission. *Opt. Express* **22**, 25295–25306 (2014).
6. A. V. Bragas, S. M. Landi, O. E. Martínez, Laser field enhancement at the scanning tunneling microscope junction measured by optical rectification. *Appl. Phys. Lett.* **72**, 2075–2077 (1998).
7. D. R. Ward, F. Hüser, F. Pauly, J. C. Cuevas, D. Natelson, Optical rectification and field enhancement in a plasmonic nanogap. *Nat. Nanotechnol.* **5**, 732–736 (2010).
8. J. Lee, X. Tu, W. Ho, Spectroscopy and microscopy of spin-sensitive rectification current induced by microwave radiation. *Nano Lett.* **5**, 2613–2617 (2005).
9. X. W. Tu, J. H. Lee, W. Ho, Atomic-scale rectification at microwave frequency. *J. Chem. Phys.* **124**, 021105 (2006).
10. W. Paul, S. Baumann, C. P. Lutz, A. J. Heinrich, Generation of constant-amplitude radio-frequency sweeps at a tunnel junction for spin resonance STM. *Rev. Sci. Instrum.* **87**, 074703 (2016).
11. T. L. Cocker, D. Peller, P. Yu, J. Repp, R. Huber, Tracking the ultrafast motion of a single molecule by femtosecond orbital imaging. *Nature* **539**, 263–267 (2016).
12. T. Choi, C. P. Lutz, A. J. Heinrich, Studies of magnetic dipolar interaction between individual atoms using ESR-STM. *Curr. Appl. Phys.* **17**, 1513–1517 (2017).
13. P. Willke, W. Paul, F. D. Natterer, K. Yang, Y. Bae, T. Choi, J. Fernández-Rossier, A. J. Heinrich, C. P. Lutz, Probing quantum coherence in single-atom electron spin resonance. *Sci. Adv.* **4**, eaaq1543 (2018).
14. P. Willke, A. Singha, X. Zhang, T. Esat, C. P. Lutz, A. J. Heinrich, T. Choi, Tuning single-atom electron spin resonance in a vector magnetic field. *Nano Lett.* **19**, 8201–8206 (2019).
15. X. Zhang, C. Wolf, Y. Wang, H. Aubin, T. Bilgeri, P. Willke, A. J. Heinrich, T. Choi, Electron spin resonance of single iron phthalocyanine molecules and role of their non-localized spins in magnetic interactions. *Nat. Chem.* **14**, 59–65 (2022).
16. L. Wang, Y. Xia, W. Ho, Atomic-scale quantum sensing based on the ultrafast coherence of an H2 molecule in an STM cavity. *Science* **376**, 401–405 (2022).
17. I. V. Pechenezhskiy, X. Hong, G. D. Nguyen, J. E. P. Dahl, R. M. K. Carlson, F. Wang, M. F. Crommie, Infrared spectroscopy of molecular submonolayers on surfaces by infrared scanning tunneling microscopy: Tetramantane on Au(111). *Phys. Rev. Lett.* **111**, 126101 (2013).

18. E. Fung, O. Adak, G. Lovat, D. Scarabelli, L. Venkataraman, Too hot for photon-assisted transport: Hot-electrons dominate conductance enhancement in illuminated single-molecule junctions. *Nano Lett.* **17**, 1255–1261 (2017).
19. M. Garg, K. Kern, Attosecond coherent manipulation of electrons in tunneling microscopy. *Science* **367**, 411–415 (2020).
20. M. Imai-Imada, H. Imada, K. Miwa, Y. Tanaka, K. Kimura, I. Zoh, R. B. Jaculbia, H. Yoshino, A. Muranaka, M. Uchiyama, Y. Kim, Orbital-resolved visualization of single-molecule photocurrent channels. *Nature* **603**, 829–834 (2022).
21. H. J. Queisser, D. E. Theodorou, Decay kinetics of persistent photoconductivity in semiconductors. *Phys. Rev. B Condens. Matter* **33**, 4027–4033 (1986).
22. C. H. Qiu, J. I. Pankove, Deep levels and persistent photoconductivity in GaN thin films. *Appl. Phys. Lett.* **70**, 1983–1985 (1997).
23. M. C. Tarun, F. A. Selim, M. D. McCluskey, Persistent photoconductivity in strontium titanate. *Phys. Rev. Lett.* **111**, 187403 (2013).
24. X. Wang, H. Gao, Distinguishing the photothermal and photoinjection effects in vanadium dioxide nanowires. *Nano Lett.* **15**, 7037–7042 (2015).
25. M. Hou, H. So, A. J. Suria, A. S. Yalamarthy, D. G. Senesky, Suppression of persistent photoconductivity in AlGaN/GaN Ultraviolet photodetectors using in Situ heating. *IEEE Electron Device Lett.* **38**, 56–59 (2017).
26. L. Wang, P. Chen, Y.-C. Wang, G.-S. Liu, C. Liu, X. Xie, J.-Z. Li, B.-R. Yang, Tape-based photodetector: Transfer process and persistent photoconductivity. *ACS Appl. Mater. Interfaces* **10**, 16596–16604 (2018).
27. M.-K. Dai, Y.-R. Liou, J.-T. Lian, T.-Y. Lin, Y.-F. Chen, Multifunctionality of giant and long-lasting persistent photoconductivity: Semiconductor–conductor transition in graphene nanosheets and amorphous ingazno hybrids. *ACS Photonics* **2**, 1057–1064 (2015).
28. S. Das, J. A. Peters, W. Lin, S. S. Kostina, P. Chen, J.-I. Kim, M. G. Kanatzidis, B. W. Wessels, Charge transport and observation of persistent photoconductivity in Tl_6SeI_4 single crystals. *J. Phys. Chem. Lett.* **8**, 1538–1544 (2017).
29. J. Reemts, A. Kittel, Persistent photoconductivity in highly porous ZnO films. *J. Appl. Phys.* **101**, 13709 (2007).
30. K. Roy, M. Padmanabhan, S. Goswami, T. P. Sai, G. Ramalingam, S. Raghavan, A. Ghosh, Graphene–MoS_2 hybrid structures for multifunctional photoresponsive memory devices. *Nat. Nanotechnol.* **8**, 826–830 (2013).
31. A. Abelenda, M. Sánchez, G. M. Ribeiro, P. A. Fernandes, P. M. P. Salomé, A. F. da Cunha, J. P. Leitão, M. I. N. da Silva, J. C. González, Anomalous persistent photoconductivity in Cu2ZnSnS4 thin films and solar cells. *Sol. Energy Mater. Sol. Cells* **137**, 164–168 (2015).
32. T.-T. Kang, P.-P. Chen, Bi_2Te_3 photoconductive detector under weak light. *J. Appl. Phys.* **126**, 83103 (2019).
33. A. Czudek, A. Urbaniak, A. Eslam, R. Wuerz, M. Igalson, Dependence of the magnitude of persistent photoconductivity on sodium content in Cu(In,Ga)Se_2 solar cells and thin films. *IEEE J. Photovoltaics* **10**, 1926–1930 (2020).
34. Y. Huang, F. Zhuge, J. Hou, L. Lv, P. Luo, N. Zhou, L. Gan, T. Zhai, Van der waals coupled organic molecules with monolayer MoS2 for fast response photodetectors with gate-tunable responsivity. *ACS Nano* **12**, 4062–4073 (2018).
35. S. Berweger, H. Zhang, P. K. Sahoo, B. M. Kupp, J. L. Blackburn, E. M. Miller, T. M. Wallis, D. V. Voronine, P. Kabos, S. U. Nanayakkara, Spatially resolved persistent photoconductivity in MoS2–WS2 lateral heterostructures. *ACS Nano* **14**, 14080–14090 (2020).
36. A. George, M. V. Fistul, M. Gruenewald, D. Kaiser, T. Lehnert, R. Mupparapu, C. Neumann, U. Hübner, M. Schaal, N. Masurkar, L. M. R. Arava, I. Staude, U. Kaiser, T. Fritz, A. Turchanin, Giant persistent photoconductivity in monolayer MoS_2 field-effect transistors. *npj 2D Mater. Appl.* **5**, 15 (2021).
37. J. Yao, P. J. Wagner, Y. Xia, G. Czap, W. Ho, Atomic-scale rectification and inelastic electron tunneling spectromicroscopy. *Nano Lett.* **22**, 7848–7852 (2022).
38. S. Li, S. Chen, J. Li, R. Wu, W. Ho, Joint space-time coherent vibration driven conformational transitions in a single molecule. *Phys. Rev. Lett.* **119**, 176002 (2017).
39. J. Gaudioso, L. J. Lauhon, W. Ho, Vibrationally mediated negative differential resistance in a single molecule. *Phys. Rev. Lett.* **85**, 1918–1921 (2000).
40. J. Gaudioso, W. Ho, Steric turnoff of vibrationally mediated negative differential resistance in a single molecule. *Angew. Chemie. Int. Ed. Engl.* **113**, 4204–4206 (2001).
41. J. Gaudioso, W. Ho, Single-molecule vibrations, conformational changes, and electronic conductivity of five-membered heterocycles. *J. Am. Chem. Soc.* **123**, 10095–10098 (2001).
42. B. C. Stipe, M. A. Rezaei, W. Ho, Inducing and viewing the rotational motion of a single molecule. *Science* **279**, 1907–1909 (1998).
43. B. McNamara, K. Wiesenfeld, Theory of stochastic resonance. *Phys. Rev. A Gen. Phys.* **39**, 4854–4869 (1989).
44. R. Löfstedt, S. N. Coppersmith, Quantum stochastic resonance. *Phys. Rev. Lett.* **72**, 1947–1950 (1994).
45. Y. Sainoo, Y. Kim, T. Okawa, T. Komeda, H. Shigekawa, M. Kawai, Excitation of molecular vibrational modes with inelastic scanning tunneling microscopy processes: Examination through action spectra of cis-2-butene on Pd(110). *Phys. Rev. Lett.* **95**, 246102 (2005).
46. K. Motobayashi, Y. Kim, H. Ueba, M. Kawai, Insight into action spectroscopy for single molecule motion and reactions through inelastic electron tunneling. *Phys. Rev. Lett.* **105**, 76101 (2010).
47. J. Oh, H. Lim, R. Arafune, J. Jung, M. Kawai, Y. Kim, Lateral hopping of CO on Ag(110) by multiple overtone excitation. *Phys. Rev. Lett.* **116**, 56101 (2016).
48. N. Nilius, N. Ernst, H.-J. Freund, Tip influence on plasmon excitations in single gold particles in an STM. *Phys. Rev. B* **65**, 115421 (2002).
49. P. Chu, D. L. Mills, Interaction of adsorbates with electric field fluctuations near surfaces: Influence of the STM tip and plasmonic effects. *Phys. Rev. B* **79**, 115435 (2009).
50. H. Böckmann, M. Müller, A. Hammud, M.-G. Willinger, M. Pszona, J. Waluk, M. Wolf, T. Kumagai, Near-field spectral response of optically excited scanning tunneling microscope junctions probed by single-molecule action spectroscopy. *J. Phys. Chem. Lett.* **10**, 2068–2074 (2019).
51. J. Klein, A. Léger, M. Belin, D. Défourneau, M. J. L. Sangster, Inelastic-electron-tunneling spectroscopy of metal-insulator-metal junctions. *Phys. Rev. B* **7**, 2336–2348 (1973).

Acknowledgments

Funding: This research was supported by the Office of Naval Research under grant no. N00014-20-1-2475. **Author contributions:** Conceptualization: W.H. and J.Y. Methodology: J.Y., Y.P., and W.H. Investigation: J.Y., Y.P., W.H., W.S., and S.C. Supervision: W.H. and J.Y. Writing—original draft: J.Y. and W.H. Writing—review and editing: J.Y., W.H., S.C., W.S., and Y.P. **Competing interests:** The authors declare that they have no competing interests. **Data and materials availability:** All data needed to evaluate the conclusions in the paper are present in the paper and/or the Supplementary Materials. The algorithms used to analyze the data are described in the Supplementary Materials.

Submitted 18 September 2023
Accepted 2 January 2024
Published 31 January 2024
10.1126/sciadv.adk9211